

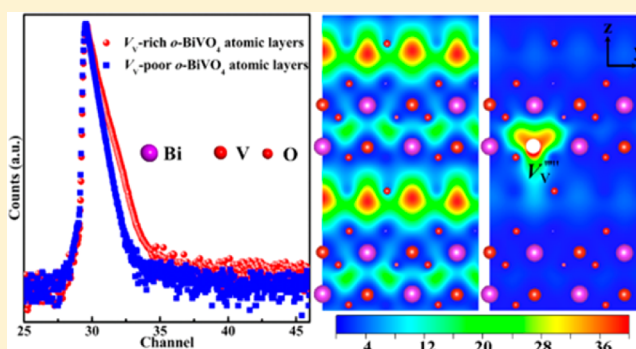
Highly Efficient and Exceptionally Durable CO₂ Photoreduction to Methanol over Freestanding Defective Single-Unit-Cell Bismuth Vanadate Layers

Shan Gao, Bingchuan Gu, Xingchen Jiao, Yongfu Sun,^{*ID} Xiaolong Zu, Fan Yang, Wenguang Zhu,^{*} Chengming Wang, Zimou Feng, Bangjiao Ye, and Yi Xie^{*ID}

Hefei National Laboratory for Physical Sciences at Microscale, CAS Center for Excellence in Nanoscience, Collaborative Innovation Center of Chemistry for Energy Materials, International Center for Quantum Design of Functional Materials, Department of Physics, Synergetic Innovation Center of Quantum Information and Quantum Physics, Key Laboratory of Strongly-Coupled Quantum Matter Physics, University of Science & Technology of China, Hefei, Anhui 230026, P. R. China

S Supporting Information

ABSTRACT: Unearthing an ideal model for disclosing the role of defect sites in solar CO₂ reduction remains a great challenge. Here, freestanding gram-scale single-unit-cell *o*-BiVO₄ layers are successfully synthesized for the first time. Positron annihilation spectrometry and X-ray fluorescence unveil their distinct vanadium vacancy concentrations. Density functional calculations reveal that the introduction of vanadium vacancies brings a new defect level and higher hole concentration near Fermi level, resulting in increased photoabsorption and superior electronic conductivity. The higher surface photovoltage intensity of single-unit-cell *o*-BiVO₄ layers with rich vanadium vacancies ensures their higher carriers separation efficiency, further confirmed by the increased carriers lifetime from 74.5 to 143.6 ns revealed by time-resolved fluorescence emission decay spectra. As a result, single-unit-cell *o*-BiVO₄ layers with rich vanadium vacancies exhibit a high methanol formation rate up to 398.3 μmol g⁻¹ h⁻¹ and an apparent quantum efficiency of 5.96% at 350 nm, much larger than that of single-unit-cell *o*-BiVO₄ layers with poor vanadium vacancies, and also the former's catalytic activity proceeds without deactivation even after 96 h. This highly efficient and spectrally stable CO₂ photoconversion performances hold great promise for practical implementation of solar fuel production.



INTRODUCTION

Worldwide consumption of finite fossil fuels not only accelerates their depletion but also results in overproduction of atmospheric CO₂ concentration, both of which will restrict social development and endanger human survival.^{1–6} In this regard, conversion of waste CO₂ into energy-rich fuels by artificial photosynthesis seems to be one of the most promising pathways for simultaneously solving the energy and environmental problems.^{6–9} Nowadays, numerous semiconductors such as TiO₂, Bi₂WO₆ and Zn₂GeO₄ have been reported for CO₂ photoreduction to form valuable chemicals,^{10–13} while their low CO₂ conversion efficiency or serious photocorrosion process greatly impede their practical implementation. Currently, several strategies have been proposed to solve these problems,^{9,14,15} in which the introduction of defects on the photocatalysts could greatly influence the photoreduction performances.⁷ However, to date, atomic-level insight into defects in photocatalytic CO₂ conversion is still an open query, which could be primarily ascribed to the following reason. In the previously fabricated photocatalysts with large crystal size, the defects usually distribute on the interior of catalysts rather

than on the surface, and thus they could not effectively involve the photocatalytic reactions. In view of disclosing the atomic-level correlation between defect sites and CO₂ photoconversion, it is obligatory to develop a material model with mainstream of defects dispensing on the surface.

Herein, we initially built an ideal material model of atomically thin layers that possess relatively single active site, and hence we deliberately create lots of defects on the surface of atomically thin layers, enabling them to behave roughly two kinds of active sites, i.e., surface sites and defect sites. The atomic thickness and two-dimensional structure make the number of these active sites comparable with their total atoms,¹⁶ thus providing new opportunities to disclose the correlation between defect sites and solar CO₂ reduction. Taking the nontoxic and stable orthorhombic-BiVO₄ (*o*-BiVO₄) as an example,¹⁷ vanadium(V)-defective *o*-BiVO₄ single-unit-cell layer and perfect *o*-BiVO₄ single-unit-cell layer slabs are built and hence density functional theory (DFT)

Received: October 28, 2016

Published: February 16, 2017

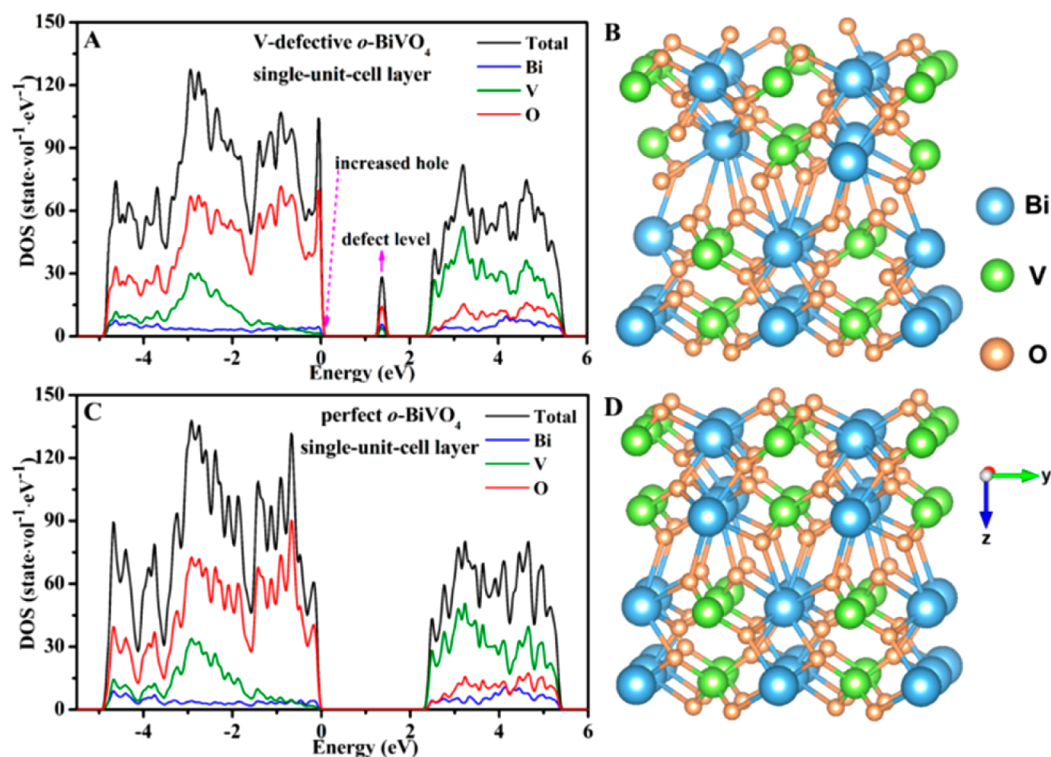


Figure 1. DFT calculations. Calculated density of states of (A) V-defective *o*-BiVO₄ single-unit-cell layer slab and (C) perfect *o*-BiVO₄ single-unit-cell layer slab along the [001] orientation. Crystal structure of (B) V-defective *o*-BiVO₄ single-unit-cell layer slab and (D) perfect *o*-BiVO₄ single-unit-cell layer slab along the [001] orientation.

calculations are performed to investigate the role of vanadium-defects on the electronic structure. Of note, Figure 1 clearly reveals that the presence of vanadium vacancies results in the appearance of a new defect level, which makes the electrons to be easily excited into the conduction band under solar irradiation, thus ensuring higher photoconversion efficiency. Moreover, one can also see that the V-defective *o*-BiVO₄ single-unit-cell layer exhibits higher hole concentration at the valence band edge in comparison with the perfect single-unit-cell layer, which infers the higher transition probability of photoexcited electrons to the conduction band under solar light illumination and hence improves the CO₂ photoreduction activity. With all of these advantages, it is rather imperative to fabricate *o*-BiVO₄ single-unit-cell layers with/without vanadium vacancies. However, since its discovery in nature as the orthorhombic mineral pucherite in 1973,¹⁷ the artificial synthesis of *o*-BiVO₄ has never been realized due to the absence of a chemically synthetic strategy, let alone the controllable synthesis of its atomic layers with desirable vanadium vacancies.

RESULTS AND DISCUSSION

To accomplish the above grant challenge, we highlight a lamellar hybrid intermediate strategy for gram-scale synthesizing V_v-rich and V_v-poor *o*-BiVO₄ atomic layers with one-unit-cell thickness, representing the first artificial synthetic case after a delay of more than 40 years. Note that cetyltrimethylammonium bromide (CTAB) played a crucial role in the formation of atomically thin layers, in which it helps to form an artificial lamellar BiCl₄⁻-CTA⁺ hybrid precursors via the self-assembly process (Figure 2A),¹⁸ confirmed by the corresponding small-angle XRD pattern in Figure S1. With the addition of Na₃VO₄ followed by hydrothermal treatment, the VO₄³⁻ ions would react with the Bi³⁺ in the lamellar BiCl₄⁻-CTA⁺ hybrid

precursors and simultaneously the formed BiVO₄-based lamellar structures gradually self-exfoliated into *o*-BiVO₄ atomic layers. Taking the products obtained at 160 °C for 3 h as an example, their XRD pattern in Figure 2C could be readily indexed to the orthorhombic-BiVO₄ (JCPDS No. 85–1730), further demonstrated by the corresponding Raman spectra in Figure S2A.¹⁹ Interestingly, compared with the relative intensity shown in the standard pattern in Figure 2C, the relatively strong 002 and 004 diffraction peaks indicated that the as-synthesized products possessed a [001] orientation. In addition, their XPS spectra and elemental mapping images in Figure S2B–D and S3 demonstrated the formation of pure BiVO₄, further verified by the corresponding IR spectrum in Figure S4,¹⁹ which suggested the absence of impurities such as CTAB and Cl⁻ on the surface of the as-obtained *o*-BiVO₄ sample. Moreover, sheet-like structures of *o*-BiVO₄ are depicted by TEM image in Figure 2B, while the atomic force microscopic (AFM) image and the corresponding height profiles in Figure 2D–E revealed their average 1.28 nm thickness, which fairly agreed with the 1.2 nm thickness of a unit cell along the [001] direction. More importantly, the weight of the final *o*-BiVO₄ ultrathin sheets are 2.184 g at one time synthesis (Figure S5), which would be beneficial for their large-scale applications. Therefore, all the above results demonstrated the gram-scale synthesis of *o*-BiVO₄ atomic layers with a thickness of a unit cell, providing new opportunities for fabricating large-area ultrathin nanodevices.

To detect the types and quantities of defects in the synthetic *o*-BiVO₄ atomic layers, positron annihilation spectrometry (PAS) was performed and the results were shown in Figure 3, Figure S9 and Tables 1 and 2. As revealed by the positron lifetime spectra in Figure 3A and the corresponding derived lifetime parameters in Table 1, the *o*-BiVO₄ atomic layers

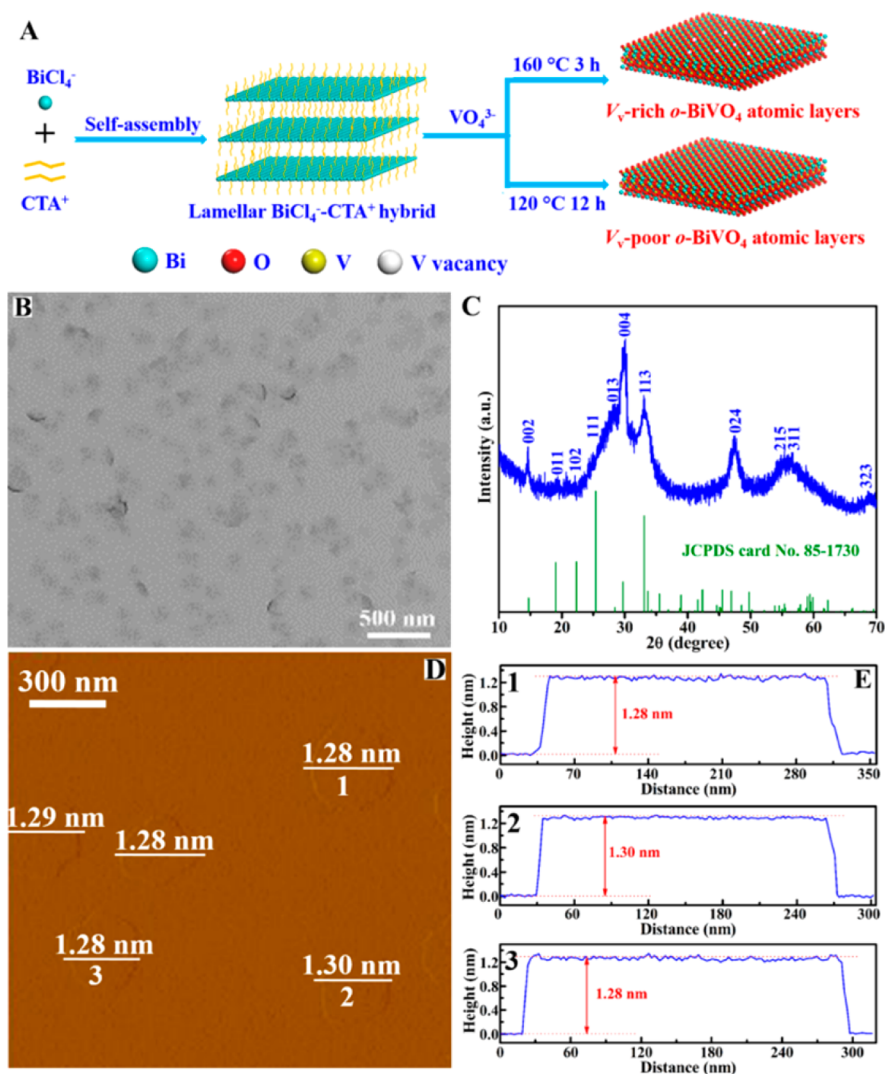


Figure 2. Scheme and characterizations for the synthetic *o*-BiVO₄ atomic layers. (A) Scheme for the gram-scale synthesis of the V_v-rich and V_v-poor *o*-BiVO₄ atomic layers. Characterizations for the V_v-rich *o*-BiVO₄ atomic layers with one-unit-cell thickness: (B) TEM image, (C) XRD pattern, (D) AFM image and (E) the corresponding height profiles; the numbers from 1 to 3 in (D) correspond to the numbers from 1 to 3 in (E).

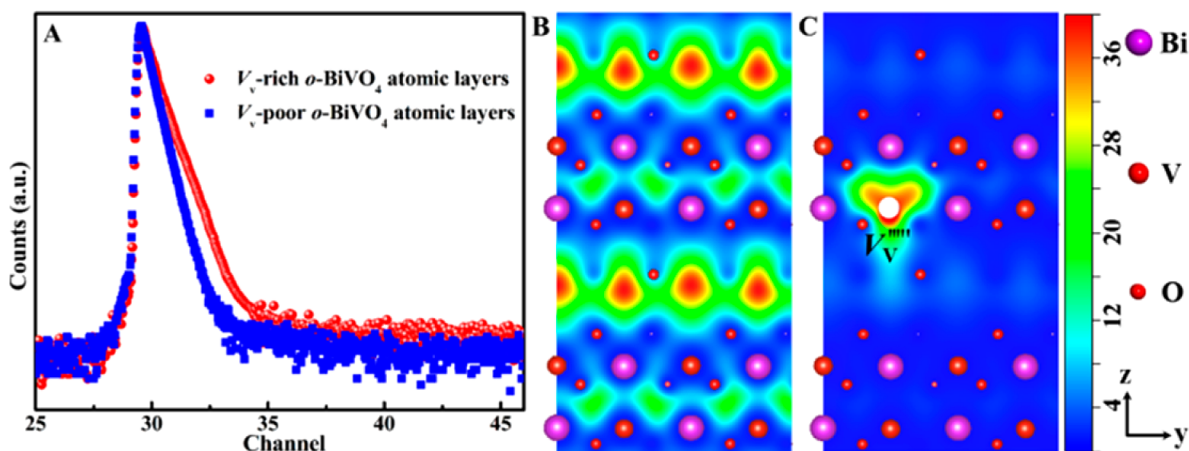


Figure 3. Defects characterization for the V_v-rich and V_v-poor *o*-BiVO₄ atomic layers. (A) Positron lifetime spectrum. (B,C) Schematic representation of trapped positrons.

exhibited three lifetime components, in which the two longer life components (τ_2, τ_3) could be ascribed to the large voids and the interface present in the samples.²⁰ Also, the shortest one

(τ_1 , around 200 ps) for the two samples could be attributed to positron annihilation trapped at vanadium vacancy of V_v^{'''}, according to the theoretically calculated positron lifetime values

Table 1. Positron Lifetime Parameters of *o*-BiVO₄ Atomic Layers^a

sample	τ_1 (ps)	τ_2 (ps)	τ_3 (ns)	I_1 (%)	I_2 (%)	I_3 (%)
V_v -poor <i>o</i> -BiVO ₄ atomic layers	200.1 ± 20	366.7 ± 3.9	2.57 ± 0.3	12.4 ± 2.9	87.7 ± 2.9	0.06 ± 0.03
V_v -rich <i>o</i> -BiVO ₄ atomic layers	208.9 ± 18	387.5 ± 2.6	2.84 ± 1.3	27.5 ± 5.7	72.3 ± 5.7	0.2 ± 0.06

^a τ_1 – τ_3 correspond to different positron lifetime in defective *o*-BiVO₄ atomic layers that have been detected in positron annihilation measurement. I_1 – I_3 are the corresponding relative intensities.

Table 2. Calculated Positron Lifetime Values of BiVO₄

defect	bulk	V_v''''	V_{Bi}''''	V_O
lifetime (ps)	193	198	236	178

in Table 2, which implied the presence of V_v'''' vacancy in these two samples. In addition to the lifetime of the positron, the relative intensity of positron lifetime also provided more information on the concentration of the defects, in which Table

1 quantified the higher vanadium vacancy concentration in the sample obtained at 160 °C for 3 h in comparison with that yielded at 120 °C for 12 h (Figure S6–S8). Importantly, as revealed by the X-ray fluorescence (XRF) in Figure S10, the element ratio of V and Bi for the V_v -rich and V_v -poor *o*-BiVO₄ atomic layers were 0.914 and 0.976, respectively, which suggested that the two samples possessed different amount of V vacancies, fairly consisting with that of the PAS measurements. This strongly demonstrated that the reaction temper-

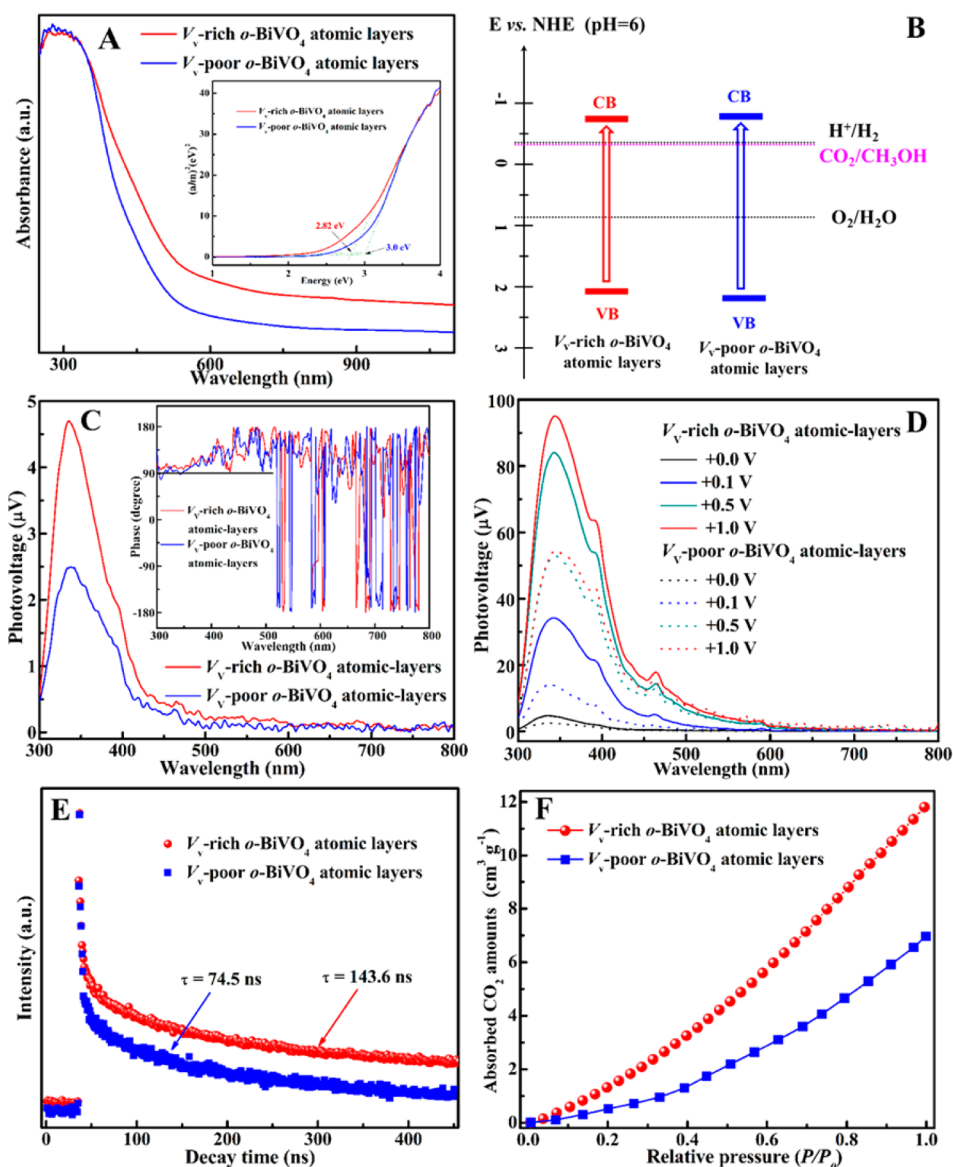


Figure 4. Photo- and electrical properties for V_v -rich and V_v -poor *o*-BiVO₄ atomic layers. (A) UV–vis diffuse reflectance spectra, (B) band positions based on the bandgaps and valence band spectra, (C) surface photovoltage spectra and (inset) corresponding phase spectra, (D) the field-induced surface photovoltage spectra under different external electric fields, (E) time-resolved fluorescence emission decay spectra, (F) CO₂ adsorption isotherms.

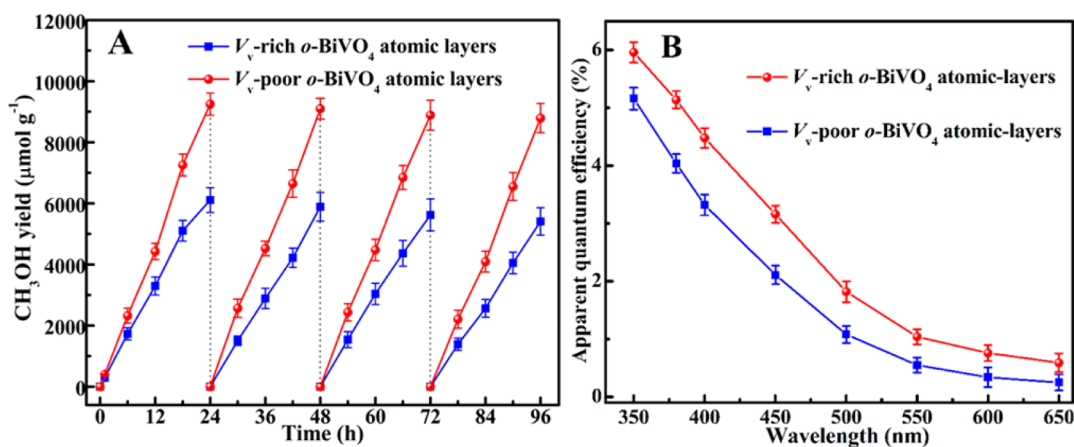


Figure 5. Photocatalytic methanol evolution under 300 W Xe lamp irradiation for V_v -rich and V_v -poor o -BiVO₄ atomic layers. (A) Photostability test and (B) apparent quantum yields. The error bars in A and B represent the standard deviations of three independent measurements of the same sample.

ature and time could help to tune the concentration of vanadium vacancy, hence providing two ideal models to study the vanadium vacancy-photocatalysis relationship.

Of note, though most monoclinic BiVO₄ like WO₃ is known to be inactive to reduce water or CO₂,^{21,22} the ultrathin thickness down to single-unit-cell layer as well as the structural defects would endow the synthetic o -BiVO₄ atomic layers with suitable electronic band structure to reduce CO₂ into methanol and simultaneously oxidize H₂O into O₂. To determine the positions of band edges relative to redox potentials of reactions, we further performed XPS valence band (VB) spectra to measure their VB position (Figure S11).²³ As shown in Figure S11, the VB maximum of V_v -poor o -BiVO₄ atomic layers is 2.48 eV, more positive than that of V_v -rich o -BiVO₄ atomic layers.^{22,24} On the basis of the band gaps in Figure 4A and the measured XPS valence band positions in Figure S11, the approximate band-edge positions of both the V_v -rich and V_v -poor o -BiVO₄ atomic layers was drawn versus a normal hydrogen electrode (NHE, pH = 6). As can be seen in Figure 4B, both the samples possessed the abilities to get both CO₂ reduction and O₂ evolution occurring at the same time.^{22,24}

As is well-known, electron–hole separation efficiency of photocatalyst is a very important factor for determining the photocatalytic activity. In this case, surface photovoltage spectroscopy (SPV) was employed to reveal the dynamic behaviors of the photogenerated charge carriers in the synthetic V_v -rich and V_v -poor o -BiVO₄ atomic layers.²⁵ Both the V_v -rich and V_v -poor o -BiVO₄ atomic layers showed a strong SPV response band in the range of 300–520 nm, which corresponded to band-to-band transition.²⁶ The increased SPV intensity for the V_v -rich o -BiVO₄ atomic layers indicated that introducing vanadium vacancies was beneficial for the separation of photogenerated electron–hole pairs in o -BiVO₄ atomic layers. Moreover, as shown in the inset of Figure 4C, the phase spectra for both the V_v -rich and V_v -poor o -BiVO₄ atomic layers showed the similar statistic kinetic characteristics in the range of 300–520 nm, and in the nonresponse range of 520–800 nm, the phase value signals were stochastic. The phase angles in the response region were in the range of +90° to +180°, indicating that photogenerated electrons and holes moved toward the surface and bulk of p-type o -BiVO₄ atomic layers, respectively.^{26,27} Hence, the photoinduced electrons accumulated at surface of the o -BiVO₄ atomic layers would be

beneficial for the activation and reduction of the surface adsorbed CO₂ molecule by a one-electron transfer. Furthermore, in the CO₂ photoreduction process, the adsorbed CO₂ and H₂O molecules were the two important reactive resources and their polarization effect on the o -BiVO₄ atomic layers would strongly affect the electron affinity as well as the surface reduction reactions. To investigate the influence of polarization effect in solar CO₂ reduction performances, we further performed the field induced surface photovoltage spectra (FISPS), in which the effect of applied voltage in the FISPS measurements was similar to the polarization effect of adsorbed CO₂ and H₂O molecules.^{26,28} As revealed in Figure 4D, one can clearly see that the SPV response intensities for both the V_v -rich and V_v -poor o -BiVO₄ atomic layers gradually increased with the increasing positive electric field, indicating that the direction of external field was consistent with that of the built-in electric field in o -BiVO₄ atomic layers, and hence further demonstrated the p-type conduction character of both the synthetic o -BiVO₄ atomic layers. Also, under the applied electric field, SPV response also appeared in the visible light range of 520–600 nm, which corresponded to the sub-band gap transition. More importantly, at the same external voltage, the V_v -rich o -BiVO₄ atomic layers exhibited much higher SPV intensities in the range of 300–600 nm than the V_v -poor o -BiVO₄ atomic layers, suggesting that the abundant vanadium vacancies ensured stronger polarization effect and hence favored much efficient separation efficiency of photoinduced charge carriers. Of note, as revealed by the CO₂ adsorption isotherms and contact angle measurements in Figure 4F and Figure S12, the V_v -rich o -BiVO₄ atomic layers possessed higher CO₂ adsorption capacity and stronger surface hydrophilicity relative to the V_v -poor o -BiVO₄ atomic layers, thanks to the former's higher vanadium vacancy concentration. Thus, the CO₂ and H₂O molecules would show stronger polarization effect on the V_v -rich o -BiVO₄ atomic layers, and hence allow for much improved photoinduced charge carrier separation efficiency. To verify the above viewpoint, time-resolved fluorescence emission decay spectra for the two samples were performed and shown in Figure 4E. The decay kinetics for V_v -rich o -BiVO₄ atomic layers, in which their respective average fluorescence lifetimes were 143.6 and 74.5 ns. The significantly increased carriers lifetime confirmed that the presence of

vanadium vacancies could effectively facilitate the separation of photogenerated electron and hole.⁹

Taking the several advantages demonstrated above, the V_v -rich o -BiVO₄ atomic layers would show remarkably promoted CO₂ photoreduction properties. To verify this viewpoint, the solar CO₂ reduction experiments were carried out in water under a 300 W Xe lamp with a standard AM 1.5G filter, and the predominant reaction product analyzed by gas chromatography (GC) was methanol, along with a small amount of H₂ as well as trace amount of ethanol (Figure S13). Control experiments demonstrated that there was no detectable methanol generation in the dark or in the absence of CO₂, verifying that the methanol formation was derived from CO₂ reduction driven by solar light irradiation. To further disclose the origin of methanol, we further performed the ¹³C labeling experiment. As shown in Figure S14, a signal corresponded to the proton was observed in the ¹H NMR spectrum (Figure S14A), while a strong signal attributed to ¹³CH₃OH was observed at 49.7 ppm in the ¹³C NMR spectrum (Figure S14B).^{29,30} These results strongly demonstrated that the methanol was in fact derived from CO₂. Figure 5A revealed that the V_v -rich o -BiVO₄ atomic layers exhibited the methanol formation rate of 398.3 μmol g⁻¹ h⁻¹, roughly 1.4 times higher than that of the V_v -poor o -BiVO₄ atomic layers, which strongly verified the crucial role of V_v vacancies in improving the photocatalytic activity. In addition, the higher vanadium vacancy amount for the V_v -rich o -BiVO₄ atomic layers also accounted for their higher apparent quantum efficiency, reaching a maximum of 5.96% at 350 nm (Figure 5B). Interestingly, the V_v -rich o -BiVO₄ atomic layers exhibited nearly the same BET surface area as that of the V_v -poor o -BiVO₄ atomic layers (Figure S15), which cannot account for the former's higher catalytic activity. This indicated that the enhanced catalytic performance of the V_v -rich o -BiVO₄ atomic layers was not due to the BET surface area, but instead the increased concentration of vanadium vacancies, which favored much higher activity toward methanol production. Moreover, the experimental results demonstrated that both the V_v -rich and V_v -poor o -BiVO₄ atomic layers could also realize the water oxidation into O₂ (Figure S16), while the rate ratio for O₂ and CH₃OH was about 1.5, which fairly agreed with the theoretical results. That is to say, the number of electron consumed for methanol, H₂ and ethanol generation was almost equal to that of electrons produced during O₂ evolution, demonstrating that the photogenerated electrons and holes simultaneously participated the respective reduction and oxidation reactions. Notably, the XRD patterns and Raman spectra in Figure S17 strongly demonstrated the phase of the V_v -rich and V_v -poor o -BiVO₄ atomic layers does not occur any obvious variation after 96 h photoreduction test, verifying their favorable photostability. More importantly, for the V_v -rich o -BiVO₄ atomic layers, their methanol yield gradually increased with the photolysis time increased up to 96 h, without showing any obvious loss of photocatalytic activity, which confirmed their superior photostability (Figure 5A). Contrastingly, the methanol yield for the V_v -poor o -BiVO₄ atomic layers increased slowly with the increasing solar irradiation, which further implied that the presence of abundant V_v vacancies ensured much better photostability, hence giving prospective signs for practical solar fuels production.

CONCLUSION

In conclusion, atomic layers with tunable defect concentrations were first put forward as an excellent platform to disclose the

atomic-level correlation between defect sites and CO₂ photoconversion. As an example, freestanding V_v -rich and V_v -poor o -BiVO₄ atomic layers with one-unit-cell thickness on gram-scale were first successfully synthesized via a lamellar hybrid intermediate strategy. Positron annihilation spectrometry and X-ray fluorescence demonstrated the distinct vanadium vacancy concentration in these fabricated o -BiVO₄ atomic layers. DFT calculation revealed that the presence of vanadium vacancies resulted in the appearance of a new defect level, which allowed for increased photoabsorption confirmed by the UV-vis diffuse reflectance spectra as well as higher apparent quantum efficiency. In addition, surface photovoltage spectroscopy disclosed that larger vanadium vacancy amount ensured higher carriers separation efficiency, confirmed by the time-resolved fluorescence spectra. The carriers lifetime for V_v -rich o -BiVO₄ atomic layers was up to 143.6 ns, roughly 2 times longer than that of V_v -poor o -BiVO₄ atomic layers. Benefiting from the above several advantages, the V_v -rich o -BiVO₄ atomic layers exhibited the high methanol formation rate up to 398.3 μmol g⁻¹ h⁻¹, roughly 1.4 times higher than that of the V_v -poor o -BiVO₄ atomic layers. Also, the catalytic activity for V_v -rich o -BiVO₄ atomic layers did not show any obvious deactivation even after 96 h-period photocatalysis, while the V_v -poor o -BiVO₄ atomic layers displayed relatively poor photostability. Accordingly, this present study not only develops a facile strategy for gram-scale fabrication of o -BiVO₄ atomic layers, but also theoretically/experimentally demonstrates the crucial role of defect sites in fully optimizing CO₂ photoreduction efficiency, opening up new possibilities for efficient and stable solar fuel production.

EXPERIMENTAL SECTION

Synthesis of V_v -rich o -BiVO₄ Atomic Layers. In a typical scalable procedure, 2.21 g BiCl₃ and 1.05 g CTAB was added into 60 mL ethylene glycol. After vigorous stirring for 40 min, 2.80 g Na₃VO₄·12H₂O was also added into the reacted system and then the mixture was transferred into a 100 mL Teflon-lined autoclave, sealed and heated at 160 °C for 3 h. The system was then allowed to cool down to room temperature naturally, the final product was collected by centrifuging the mixture, washed with ethanol and water for many times, and then dried in vacuum overnight for further characterization. More importantly, the yield of the products was only dependent on the volume of the Teflon-lined autoclave.

Synthesis of V_v -poor o -BiVO₄ Atomic Layers. In a typical scalable procedure, 2.21 g BiCl₃ and 1.05 g CTAB was added into 60 mL ethylene glycol. After vigorous stirring for 40 min, 2.80 g Na₃VO₄·12H₂O was also added into the reacted system and then the mixture was transferred into a 100 mL Teflon-lined autoclave, sealed and heated at 120 °C for 12 h. The system was then allowed to cool down to room temperature naturally, the final product was collected by centrifuging the mixture, washed with ethanol and water for many times, and then dried in vacuum overnight for further characterization. More importantly, the yield of the products was only dependent on the volume of the Teflon-lined autoclave.

Characterization. Transmission electron microscopy (TEM) images and high-resolution TEM image were performed by using a JEOL-2010 TEM with an acceleration voltage of 200 kV. XRD patterns were recorded by using a Philips X'Pert Pro Super diffractometer with Cu Kα radiation (λ = 1.54178 Å). X-ray photoelectron spectra (XPS) were acquired on an ESCALAB MKII with Mg Kα (hν = 1253.6 eV) as the excitation source. The binding energies obtained in the XPS spectral analysis were corrected for specimen charging by referencing C 1s to 284.8 eV. Room-temperature UV-vis diffuse reflectance spectroscopy (DRS) were recorded on a PerkinElmer Lambda 950 UV-vis-NIR spectrophotometer. Raman spectra were detected by a RenishawRM3000 Micro-

Raman system. The Fourier transform infrared (FT-IR) spectra were acquired on a NICOLET FT-IR spectrometer in a KBr tablets, scanning from 4000 to 400 cm^{-1} at room temperature. Elemental analysis for the products was performed on an XRF-1800. The decay time spectra were recorded on a spectrophotometer (FLS920, Edinburgh Instruments Ltd.). Decay curves for the two α - BiVO_4 atomic layers were recorded with excitation at 400 nm and emission at 525 nm. The surface photovoltage spectroscopy (SPV) and Field-induced surface photovoltage spectroscopy (FISPS) measurements were carried out on a homemade apparatus, which was constituted by a source of monochromatic light with a light chopper, and a lock-in amplifier. The measurement was performed in air atmosphere and room temperature. Atomic force microscopy (AFM) study in the present work was performed as follows: Mica sheet was initially fixed on the surface of nickel substance and then the up surface of the Mica sheet was stripped by tape. When the up surface of Mica sheet was flat uniformly, 50 μL colloidal dispersion (2 mg sample was uniformly dispersed into 10 mL ethanol or water under ultrasonication) was dropped by Micro syringe on the flat surface of Mica sheet and then dried in air naturally for further AFM characterization (Veeco DI Nanoscope MultiMode V system).

Density Functional Theory Calculations. were performed using the Vienna ab initio simulation package (VASP) with projector-augmented wave (PAW) pseudopotentials and the generalized gradient approximation in the parametrization of Perdew, Burke and Enzerhof for the exchange-correlation functional.^{31–34} Bi 5d6s6p electrons, V 3s3p3d4s electrons, and O 2s2p electrons were treated as the valence electrons in the PAW potentials. The plane-wave energy cutoff, 400 eV, was determined by the VASP PAW potential of O. All atoms fully relaxed during structural relaxation until the force on each atom was smaller than 0.01 eV/Å. The lattice parameters of the optimized orthorhombic phase BiVO_4 are $a = 5.393$ Å, $b = 5.093$ Å, and $c = 12.088$ Å, in consistent with the experimental values of $a = 5.328$ Å, $b = 5.052$ Å, and $c = 12.003$ Å. The 2D BiVO_4 thin film was model by a $2 \times 2 \times 1$ cell with a vacuum region over 13 Å containing 16 Bi, 16 V, and 64 O atoms. We used a $7 \times 7 \times 1$ k-point mesh including the Γ point for the Brillouin Zone integration.

Photocatalytic CO_2 Reduction Measurement. In the photocatalytic conversion of CO_2 , BiVO_4 powder (0.2 g) was suspended in 160 mL water with magnetic stirring, and high purity CO_2 gas was continuously bubbled through the solution at the rate of 0.5 mL min^{-1} . A 300 W Xe lamp (PLS-SXE300/300UV, Trusttech Co., Ltd. Beijing) with a standard AM1.5 filter, outputting the light density of about 100 mW/cm^2 , was used as the light source. The photocatalytic CO_2 reduction experiments were conducted in a closed vessel at 0 °C, and the suspensions were irradiated through the quartz window. Prior to irradiation, CO_2 gas was bubbled to the solution for 30 min to expel the dissolved oxygen in the vessel. The vessel temperature was kept at about 0 °C by recirculating cooling water system to increase the solubility of CO_2 . The products in the solution were qualitatively identified by gas chromatography (SP6800A with GDX-502 columns) equipped with a flame ionization detector (FID), and the outlet gases were sampled through a sampling valve and analyzed by gas chromatography (SP6800A with TDX-01 columns) equipped with thermal conductivity detector (TCD). All peaks were checked with their corresponding standards, and each experiment was repeated at least 5 times in parallel to obtain an average value. The wavelength-dependent apparent quantum yields (AQY) was measured under the same photocatalytic reaction condition, except for the incident light wavelength. The solar fuels (methanol) yields of 10 h photoreaction under different monochromatic light wavelengths (350, 380, 400, 450, 500, 550, 600, and 650 nm) were measured. All the fwhm of these wavelengths were 10 nm. The temperatures of the solutions were controlled at 273 ± 0.2 K by recirculating cooling water system during irradiation. The incident light intensity was determined using a Silicon-UV enhanced actinometer. The wavelength-dependent AQY was calculated as the ratio between the number of photogenerated electrons consumption and the number of incident photons, by taking into account the fact that 6 electrons are required according to the stoichiometry of the reaction: $\text{CO}_2 + 2\text{H}_2\text{O} \rightarrow \text{CH}_3\text{OH} + 3/2\text{O}_2$. All

the experiments were repeated at least 5 times in parallel to obtain an average value.

Positron Annihilation Measurement. The positron lifetime measurements were carried out with a fast–fast coincidence system with a time resolution of ~ 240 ps full width at half-maximum. Each spectrum was collected with a total count of 1×10^6 . A 30 μCi source of ^{22}Na was sandwiched between two identical BiVO_4 samples. All the samples were measured at least 3 times in parallel to obtain an average value. To obtain the positron lifetimes, the ATSUP method and the GGA (Generalized Gradient Approximation) form of the enhancement factor were chosen.^{35,36} The electron density and the positron crystalline Coulomb potential were constructed by the nonself-consistent superposition of free atom electron density and Coulomb potential in the absence of the positron. The model of $3 \times 3 \times 2$ supercells were used for Positron lifetime calculations of 2D BiVO_4 with unrelaxed structure vacancy.

The specific fitting parameters for both V_r -poor and V_r -rich α - BiVO_4 atomic layers are also shown in the Figure S9. According to the LTV9 program, the primitive spectra can be decomposed to five components. Two of them come from source contribution including the annihilation in source itself (NaCl) and the Kapton film which are used to cover the source. The line in dark yellow and purple are attributed to these two components obtained by measuring a single crystal silicon. The left three components indicated by dark gray, blue, and black lines are attributed to the samples, which correspond to around 200 ps, 370 ps, and more than 2 ns, respectively. Moreover, the fitting residuals are also shown in the bottom of the picture (olive lines). The uniformity of these scatter plots imply the rationality of this fitting.

■ ASSOCIATED CONTENT

Supporting Information

The Supporting Information is available free of charge on the ACS Publications website at DOI: 10.1021/jacs.6b11263.

Positron Annihilation measurement, yields of various products, ^{13}C labeling experiment, details of XRD, XPS, XRF, Raman, FT-IR, BET surface area, Elemental mapping images, XPS valence band spectrum, contact angles, TEM and AFM image, as well as supplementary demonstration of gram-scale synthesis (PDF)

■ AUTHOR INFORMATION

Corresponding Authors

*yfsun@ustc.edu.cn

*wgzhu@ustc.edu.cn

*yxie@ustc.edu.cn

ORCID

Yongfu Sun: 0000-0002-4420-5708

Yi Xie: 0000-0002-1416-5557

Notes

The authors declare no competing financial interest.

■ ACKNOWLEDGMENTS

This work was financially supported by the National Natural Science Foundation of China (21422107, U1632147, 91422303, 21331005, 21201157, 11321503, 21173205, 91127042, 11374273, 11674299, 11634011), Key Research Program of Frontier Sciences, CAS (QYZDY-SSW-SLH011), the Chinese Academy of Sciences (XDB01020000), the Program for New Century Excellent Talents in University (NCET-13-0546), the Youth Innovation Promotion Association of CAS (CX2340000100), the Fundamental Research Funds for the Central Universities (WK2340000063), and Scientific Research Grant of Hefei Science Center of CAS

(2016HSC-IU002), National Postdoctoral Program for Innovative Talents (BX201600143). China Postdoctoral Science Foundation Funded project (2016M602017). Supercomputing center of USTC is acknowledged for computational support.

REFERENCES

- (1) Lin, S.; Diercks, C. S.; Zhang, Y. P.; Kornienko, N.; Nichols, E. M.; Zhao, Y. B.; Paris, A. R.; Kim, D.; Yang, P. D. *Science* **2015**, *349*, 1208.
- (2) Cao, Z.; Kim, D.; Hong, D. C.; Yu, Y.; Xu, J.; Lin, S.; Wen, X. D.; Nichols, E. M.; Jeong, K.; Reimer, J. A.; Yang, P. D.; Chang, C. J. *J. Am. Chem. Soc.* **2016**, *138*, 8120.
- (3) Gao, S.; Lin, Y.; Jiao, X. C.; Sun, Y. F.; Luo, Q. Q.; Zhuang, W. H.; Li, D. Q.; Yang, J. L.; Xie, Y. *Nature* **2016**, *529*, 68.
- (4) Gao, S.; Jiao, X. C.; Sun, Z. T.; Zhang, W. H.; Sun, Y. F.; Wang, C. M.; Hu, Q. T.; Zu, X. L.; Yang, F.; Yang, S. Y.; Liang, L.; Wu, J.; Xie, Y. *Angew. Chem., Int. Ed.* **2016**, *55*, 698.
- (5) Kim, D.; Resasco, J.; Yu, Y.; Asiri, A. M.; Yang, P. D. *Nat. Commun.* **2014**, *5*, 4948.
- (6) Thoi, V. S.; Kornienko, N.; Margarit, C. G.; Yang, P. D.; Chang, C. J. *J. Am. Chem. Soc.* **2013**, *135*, 14413.
- (7) Zhang, L.; Wang, W. Z.; Jiang, D.; Gao, E. P.; Sun, S. M. *Nano Res.* **2015**, *8*, 821.
- (8) Izumi, Y. *Coord. Chem. Rev.* **2013**, *257*, 171.
- (9) Liang, L.; Lei, F. C.; Gao, S.; Sun, Y. F.; Jiao, X. C.; Wu, J.; Qamar, S.; Xie, Y. *Angew. Chem., Int. Ed.* **2015**, *54*, 13971.
- (10) Wang, W. N.; An, W. J.; Ramalingam, B.; Mukherjee, S.; Niedzwiedzki, D. M.; Gangopadhyay, S.; Biswas, P. J. *J. Am. Chem. Soc.* **2012**, *134*, 11276.
- (11) Cheng, H. F.; Huang, B. B.; Liu, Y. Y.; Wang, Z. Y.; Qin, X. Y.; Zhang, X. Y.; Dai, Y. *Chem. Commun.* **2012**, *48*, 9729.
- (12) Yan, S. C.; Wan, L. J.; Li, Z. S.; Zou, Z. G. *Chem. Commun.* **2011**, *47*, 5632.
- (13) Mao, J.; Peng, T. Y.; Zhang, X. H.; Li, K.; Zan, L. *Catal. Commun.* **2012**, *28*, 38.
- (14) An, X. Q.; Li, K. F.; Tang, J. W. *ChemSusChem* **2014**, *7*, 1086.
- (15) Wang, Y. G.; Wang, F.; Chen, Y. T.; Zhang, D. F.; Li, B.; Kang, S. F.; Li, X.; Cui, L. F. *Appl. Catal., B* **2014**, *147*, 602.
- (16) Sun, Y. F.; Gao, S.; Lei, F. C.; Xie, Y. *Chem. Soc. Rev.* **2015**, *44*, 623.
- (17) Knorring, O. V.; Sahama, T. G.; Lehtinen, M.; Rehtijärvi, P.; Siivola, J. *Contrib. Mineral. Petrol.* **1973**, *41*, 325.
- (18) Wang, J. W.; Li, Y. D. *Adv. Mater.* **2003**, *15*, 445.
- (19) Frost, R. L.; Henry, D. A.; Weier, M. L.; Martens, W. J. *Raman Spectrosc.* **2006**, *37*, 722.
- (20) Guan, M. L.; Xiao, C.; Zhang, J.; Fan, S. J.; An, R.; Cheng, Q. M.; Xie, J. F.; Zhou, M.; Ye, B. J.; Xie, Y. *J. Am. Chem. Soc.* **2013**, *135*, 10411.
- (21) Sun, S. M.; Wang, W. Z.; Li, D. Z.; Zhang, L.; Jiang, D. *ACS Catal.* **2014**, *4*, 3498.
- (22) Xie, Y. P.; Liu, G.; Yin, L. C.; Cheng, H. M. *J. Mater. Chem.* **2012**, *22*, 6746.
- (23) Guo, S. E.; Deng, Z. P.; Li, M. X.; Jiang, B. J.; Tian, C. G.; Pan, Q. J.; Fu, H. G. *Angew. Chem., Int. Ed.* **2016**, *55*, 1830.
- (24) Chen, X. Y.; Zhou, Y.; Liu, Q.; Li, Z. D.; Liu, J. G.; Zou, Z. G. *ACS Appl. Mater. Interfaces* **2012**, *4*, 3372.
- (25) Jing, L. Q.; Zhou, W.; Tian, G. H.; Fu, H. G. *Chem. Soc. Rev.* **2013**, *42*, 9509.
- (26) Fan, H. M.; Wang, D. J.; Wang, L. L.; Li, H. Y.; Wang, P.; Jiang, T. F.; Xie, T. F. *Appl. Surf. Sci.* **2011**, *257*, 7758.
- (27) Ivanov, D. V.; Germanova, K.; Kirilov, K. J. *Phys. D: Appl. Phys.* **2009**, *42*, 135302.
- (28) Zhang, G. Q.; Jiang, W. S.; Hua, S. X.; Zhao, H. F.; Zhang, L. G.; Sun, Z. C. *Nanoscale* **2016**, *8*, 16963.
- (29) Fulmer, G. R.; Miller, A. J. M.; Sherden, N. H.; Gottlieb, H. E.; Nudelman, A.; Stoltz, B. M.; Bercaw, J. E.; Goldberg, K. I. *Organometallics* **2010**, *29*, 2176.
- (30) Kuhl, K. P.; Cave, E. R.; Abram, D. N.; Jaramillo, T. F. *Energy Environ. Sci.* **2012**, *5*, 7050.
- (31) Kresse, G.; Furthmüller, J. *Phys. Rev. B: Condens. Matter Mater. Phys.* **1996**, *54*, 11169.
- (32) Blöchl, P. E. *Phys. Rev. B: Condens. Matter Mater. Phys.* **1994**, *50*, 17953.
- (33) Kresse, G.; Joubert, D. *Phys. Rev. B: Condens. Matter Mater. Phys.* **1999**, *59*, 1758.
- (34) Perdew, J. P.; Burke, K.; Ernzerhof, M. *Phys. Rev. Lett.* **1996**, *77*, 3865.
- (35) Robles, J. M. C.; Ogando, E.; Plazaola, F. J. *Phys.: Condens. Matter* **2007**, *19*, 176222.
- (36) Barbiellini, B.; Puska, M. J.; Korhonen, T.; Harju, A.; Torsti, T.; Nieminen, R. M. *Phys. Rev. B: Condens. Matter Mater. Phys.* **1996**, *53*, 16201.